International Journal of Mechanical Sciences 261 (2024) 108694

Contents lists available at ScienceDirect

International Journal of Mechanical Sciences

journal homepage: www.elsevier.com/locate/ijmecsci

An implicit immersed boundary method for Robin boundary condition

Buchen Wu [a,b], Chang Shu [a,*], Minping Wan [b,c,d,**]

[a] Department of Mechanical Engineering, National University of, Singapore, 10 Kent Ridge Crescent, Singapore, 119260, Singapore
[b] Guangdong Provincial Key Laboratory of Turbulence Research and Applications, Department of Mechanics and Aerospace Engineering, Southern University of Science and Technology, Shenzhen, 518055, Guangdong, China
[c] Guangdong-Hong Kong-Macao Joint Laboratory for Data-Driven Fluid Mechanics and Engineering Applications, Southern University of Science and Technology, Shenzhen, 518055, Guangdong, China
[d] Jiaxing Research Institute, Southern University of Science and Technology, Jiaxing, 314031, Zhejiang, China

ARTICLE INFO

Keywords:
Immersed boundary method
Robin boundary condition
Thermal flow

ABSTRACT

In this work, a novel boundary condition-enforced immersed boundary method (IBM) for simulating complex thermal–fluid–structure interaction (TFSI) problems with Robin boundary conditions is proposed. In this work, two auxiliary layers of Lagrangian points are introduced and placed within the inner and outer parts of the immersed object to enable the simultaneous evaluation of the temperature and its gradient on the solid surface. The mutual thermal interactions between the immersed object and the surrounding flow are taken into account through the temperature corrections on the Lagrangian points by accurately enforcing the Robin boundary condition on the solid boundary. Hence, a system of linear equations can be formulated to compute the temperature corrections. Subsequently, the temperature corrections are biasedly distributed to the Eulerian points located in the inner auxiliary layer to eliminate the diffusion generated by the smooth delta function on the temperature field outside the solid object. The proposed IBM integrated with the reconstructed thermal lattice Boltzmann flux solver (RTLBFS) is extensively and critically assessed with classical benchmark cases ranging from two-dimensional stationary problems to three-dimensional problems involving moving boundaries to demonstrate the robustness and accuracy of the proposed method for Robin boundary conditions. Results from the present work are extensively corroborated with previous works that adopt different approaches for imposing the Robin boundary condition. It shows that the proposed method not only provides a much more accurate representation of the Robin boundary condition but also introduces a simple implementation for the complex Robin boundary condition within the diffuse interface IBM framework.

1. Introduction

The immersed boundary method (IBM) [1–5] has always been attractive, owing to its simplicity yet robustness for resolving thermal-fluid–structure interaction (TFSI) problems with complex geometries and moving boundaries on simple Cartesian meshes. The methodology of the IBM was firstly introduced by Peskin [6] to investigate the blood flow problem. In contrary to conventional numerical approaches adopting body-fitted meshes, IBMs introduce a set of Lagrangian points to facilitate the information exchange between solid boundary and surrounding flows, thereby, removing tedious mesh generation requirement when simulating flows around moving immersed objects. Therefore, tremendous efforts have been placed on developing various accurate and efficient IBMs for handling various types of boundary conditions.

Generally, there are three types of boundary conditions found in practical TFSI problems, namely, Dirichlet boundary condition, Neumann boundary condition, and Robin boundary condition. Various IBMs have been developed to simulate flows with Dirichlet boundary condition [6–25] and Neumann boundary condition [26–39]. For Dirichlet boundary condition, IBMs can be categorized into: the penalty forcing scheme [6,14], the direct forcing scheme [15–17], the feedback forcing scheme [12,13], the momentum exchange scheme [18,19], and the boundary condition-enforced scheme [7,11,21,23]. Among these IBMs, the boundary condition-enforced IBMs [7,11,21,23,40] have been widely applied to simulate complex fluid structure problems [41–45], since it can accurately impose Dirichlet boundary condition on the solid boundary. For Neumann boundary condition, IBMs can be divided into two groups: (i) the explicit scheme [26,29,34,38] that calculates the temperature correction by introducing a heat source,

* Corresponding author.
** Correspondence to: Department of Mechanics and Aerospace Engineering, Southern University of Science and Technology.
E-mail addresses: mpeshuc@nus.edu.sg (C. Shu), wanmp@sustech.edu.cn (M. Wan).

https://doi.org/10.1016/j.ijmecsci.2023.108694
Received 20 June 2023; Received in revised form 15 August 2023; Accepted 22 August 2023
Available online 26 August 2023
0020-7403/© 2023 Elsevier Ltd. All rights reserved.

which is similar to the penalty forcing scheme or direct forcing scheme for Dirichlet boundary condition; (ii) the implicit scheme [33] that directly evaluates the temperature correction on Lagrangian points by accurately imposing the Neumann boundary condition on the immersed object. While the Dirichlet and Neumann boundary conditions are well researched and established, the boundary condition of practical engineering problems is more complex and is a combination of Dirichlet and Neumann boundary conditions, namely, Robin boundary condition. Robin boundary conditions are normally found in conjugate heat transfer problems.

In contrast to Dirichlet boundary condition and Neumann boundary condition, it is much more challenging to develop an IBM to accurately fulfill Robin boundary condition on the solid boundary [4,46]. There are only a handful of IBMs [47–52] that have been proposed for implementing the Robin boundary condition. Pacheco-Vega et al. [48] converted the boundary effects to the restoring forcing terms through direct forcing scheme, where they proposed a general interpolation scheme to obtain the temperature and its gradient on the solid boundary. Subsequently, Kinoshita et al. [53] extended this numerical scheme [48] in the framework of the Fourier pseudospectral method. Kumar and Natarajan [54] and Favre et al. [55] proposed a volume-of-solid IBM for Robin boundary conditions in the framework of diffuse interface IB, but this numerical scheme suffers severe spurious force oscillations (SFO), triggering the oscillatory Nusselt number distributions. Pan et al. [56] developed a unified form IBM based on a high order least square interpolation reconstruction, which falls into the sharp interface IB's framework and requires complex point identification algorithms. Most of IBMs for Robin boundary conditions are based on the ghost cell immersed boundary method (GCIBM) originally proposed by Mohd-Yusof [57] and Fadlun et al. [58]. Tseng and Ferziger [47] proposed a GCIBM for simulating fluid–structure interaction problems with three boundary conditions by using second-order ghost cell reconstruction. Pan [49] introduced projection points and image points in GCIBM to calculate the variable value and its gradient for implicitly satisfying the boundary condition at the projection point. Then, Luo et al. [50,51,59] proposed a second-order reconstruction scheme for resolving Robin type heat transfer problems by interpolating the flow variables on the mirror point with four surrounding fluid points. Subsequently, Yousefzadeh and Battiato [52] developed a high order GCIBM with a compact interpolation stencil to avoid unnecessary extension of the discretization stencil and remove the arbitrary choice of the distance between the mirror point and boundary. Recently, Ou et al. [60] proposed a directional GCIBM for Robin boundary condition, where the variables at ghost points are separately reconstructed along each discretization direction. However, these IBMs based on the GCIBM have to identify the fluid point, solid point, ghost point, and mirror point at each time step when simulating the flow around moving objects; in addition, the flow variables at these points are evaluated through different interpolation methods, increasing computational complexity. Therefore, it is complicated to practically implement these GCIBMs to handle Robin type problems with complex geometries. Furthermore, these GCIBMs evaluate the temperature correction by introducing a boundary thermal forcing term rather than directly solving the temperature correction.

In this work, to effectively simulate TFSI problems with Robin boundary condition, a novel boundary condition-enforced immersed boundary method is proposed, where the temperature corrections on the Lagrangian points are implicitly resolved by accurately fulfilling the Robin boundary condition on the immersed object. To evaluate the temperature gradient with second order accuracy, two layers Lagrangian points are introduced and respectively placed inside and outside of the immersed object with two Eulerian grid spacings. The boundary effects on the immersed object and surrounding flows are directly converted to the unknown temperature corrections on Lagrangian points, which are biasedly distributed on the Eulerian points inside the inner layer to eliminate the diffusion introduced by the delta function on the temperature field outside the solid body. This biased distribution of the temperature corrections is inspired by previous works [33,61], where a biased distribution can successfully impose Dirichlet and Neumann boundary conditions on the solid body. The proposed IBM coupled with the RTLBFS [62] will be validated in detail by conducting some benchmarks of forced convection with stationary and moving objects. Furthermore, the present approach is extended to simulate complex moving boundary and three dimensional problems.

The paper is organized as follows: the mathematical formulations, the numerical approaches for thermal flows, and the IBM for Dirichlet boundary conditions are introduced in Section 2. In Section 3, the methodology of the novel boundary condition-enforced IBM for Robin boundary conditions are presented. In Section 4, we assessed the overall numerical accuracy of the present method and conducted numerical validations of the boundary condition-enforced IBM for Robin boundary condition. Specifically, Sections 4.2–4.3 demonstrate the capability of the proposed IBM for resolving the Robin type TFSI problems with stationary and moving boundary. Sections 4.4–4.5 extend the proposed method for TFSI problems involving complex moving boundaries in two and three-dimensional spatial spaces. Conclusions are drawn in Section 5.

2. The mathematical model and numerical approach

In this section, the governing equations and numerical methods for TFSI problems are described. Briefly, a fractional step method is employed to decompose the solution of Navier–Stokes equations into a predictor–corrector step. In the predictor step, the RTLBFS [62] is used to predict the intermediate flow and temperature fields without taking into account the effects induced by the immersed object. Subsequently, in the corrector step, different IBMs are adopted to impose the no-slip boundary condition and Robin boundary condition on the solid wall.

2.1. Navier–Stokes (N-S) equations

For general thermal viscous flows, the macroscopic governing equations of mass, momentum and energy conservation laws can be given as:

$$\frac{\partial \rho}{\partial t} + \nabla \cdot (\rho \mathbf{u}) = 0, \tag{1a}$$

$$\frac{\partial (\rho \mathbf{u})}{\partial t} + \nabla \cdot (\rho \mathbf{u}\mathbf{u}) = -\nabla p + \nu \nabla \cdot \left[\nabla \rho \mathbf{u} + (\nabla \rho \mathbf{u})^T\right] + \mathbf{F}_B + \mathbf{f}, \tag{1b}$$

$$\frac{\partial \left(\rho c_p T\right)}{\partial t} + \nabla \cdot (\rho c_p T \mathbf{u}) = \chi \nabla^2 (\rho c_p T) + q, \tag{1c}$$

where ρ, $\mathbf{u}$, ν, p, T, c_p, and χ are the density, velocity, kinematic viscosity, pressure, temperature, specific heat capacity at constant pressure, and the thermal diffusivity, respectively. The buoyancy force can be described with the aid of the Boussinesq approximation [63] as $\mathbf{F}_B = (0, 0, -\rho\zeta g(T - T_m))$, where ζ, g and T_m represent the thermal expansion coefficient, gravitational acceleration, and mean temperature, respectively. $\mathbf{f}$ is the restoring forcing term and q is the heat source term. The above N-S equations are suitable for simulating incompressible thermal viscous flows with small density variation and low Mach number limit.

2.2. RTLBFS for the intermediate flow field

In the present work, the RTLBFS is adopted to resolve the macroscopic governing equations described in Section 2.1 to determine the intermediate flow variables without taking into account the effects induced by the immersed objects. Hence, Eq. can be rewritten in a vector form:

$$\frac{\partial \mathbf{W}}{\partial t} + \nabla \cdot \mathbf{F} = 0, \tag{2}$$

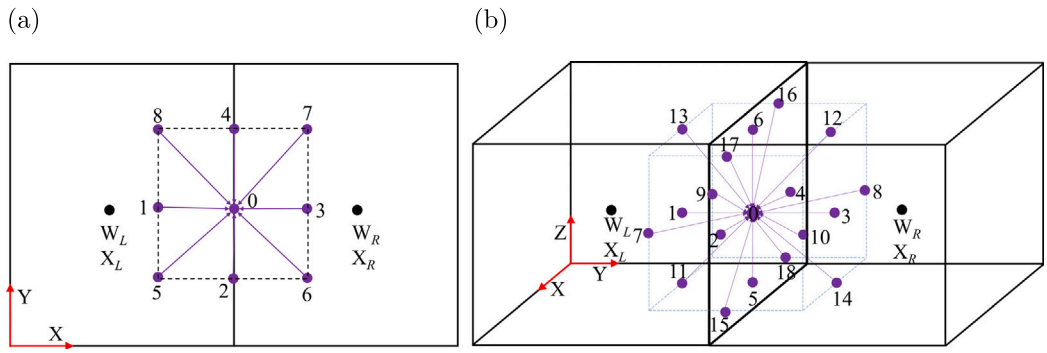

Fig. 1. Local reconstructed unit lattice (a) D2Q9 and (b) D3Q19 at the cell interface. The black points are the two adjacent cell centers and the purple points are the unit lattice points. The fluid velocity and temperature at the unit cell point are interpolated by the flow variables at the two cell centers.

where

$$\mathbf{W}=\begin{Bmatrix}\rho\\ \rho\mathbf{u}\\ \rho c_p T\end{Bmatrix},\quad \mathbf{F}=\begin{Bmatrix}\mathbf{P}\\ \mathbf{\Pi}\\ \mathbf{Q}\end{Bmatrix}, \tag{3a}$$

$$\boldsymbol{P}=\rho\mathbf{u}, \tag{3b}$$

$$\mathbf{\Pi}=\rho\mathbf{u}\mathbf{u}+p\boldsymbol{I}-\nu\left(\nabla\rho\mathbf{u}+(\nabla\rho\mathbf{u})^T\right), \tag{3c}$$

$$\mathbf{Q}=\rho c_p T\mathbf{u}-\chi\nabla(\rho c_p T). \tag{3d}$$

Note that the buoyancy force $\mathbf{F}_B$ is calculated in the intermediate step shown in Eq. (7) rather than in the flux term $\mathbf{\Pi}$.

A unit lattice is reconstructed at the cell interface as shown in Fig. 1 to obtain the interface fluxes. Hence, the flow variables ρ, $\mathbf{u}$ and T at each lattice node can be obtained by the following interpolation scheme as:

$$\mathbf{W}=\begin{cases}\mathbf{W}_L+\nabla\mathbf{W}_L\cdot\left(\mathbf{X}_N-\mathbf{X}_L\right),\mathbf{X}_N \text{ locates at the left cell;}\\ \mathbf{W}_R+\nabla\mathbf{W}_R\cdot\left(\mathbf{X}_N-\mathbf{X}_R\right),\mathbf{X}_N \text{ locates at the right cell;}\\ 0.5\left[\mathbf{W}_L+\nabla\mathbf{W}_L\cdot\left(\mathbf{X}_N-\mathbf{X}_L\right)+\mathbf{W}_R+\nabla\mathbf{W}_R\cdot\left(\mathbf{X}_N-\mathbf{X}_R\right)\right],\\ \qquad\qquad \mathbf{X}_N \text{ locates at the interface;}\end{cases} \tag{4}$$

where $\mathbf{X}_L$ and $\mathbf{X}_R$ denote the positions of the left cell center and right cell center, respectively. Note that the superscripts n, $*$, m, and $n+1$ represent the current, the sub-intermediate, the intermediate, and the next time steps, respectively.

Subsequently, the sub-intermediate flow variables ρ^*, $(\rho u_\alpha)^*$, and $(\rho T)^*$ at the cell interface are obtained through the macroscopic density and momentum equations that are recovered from the local thermal LBM as follow:

$$\rho^*=\rho^n-\partial_\alpha\left(\rho u_\alpha\right)^n\delta t+\frac{1}{2}\delta t^2\partial_\alpha\partial_\beta\left(\rho u_\alpha u_\beta+\rho c_s^2\delta_{\alpha\beta}\right)^n+O\left(\delta t^3\right), \tag{5a}$$

$$\begin{aligned}\left(\rho u_\alpha\right)^*=&\left(\rho u_\alpha\right)^n-\delta t\partial_\beta\left(\rho u_\alpha u_\beta+\rho c_s^2\delta_{\alpha\beta}\right)^n\\&+0.5c_s^2\delta t^2\partial_\beta\left[\partial_\beta\left(\rho u_\alpha\right)+\partial_\alpha\left(\rho u_\beta\right)+\partial_\gamma\left(\rho u_\gamma\right)\delta_{\alpha\beta}\right]^n+O\left(\delta t^3\right),\end{aligned} \tag{5b}$$

$$\left(\rho c_pT\right)^*=\left(\rho c_pT\right)^n-\delta t\partial_\alpha\left(\rho c_pu_\alpha T\right)^n+0.5c_s^2\delta t^2\partial_\alpha\partial_\beta\left(\rho c_pT\delta_{\alpha\beta}\right)^n+O\left(\delta t^3\right), \tag{5c}$$

where subscripts α, β and γ are the coordinate components. c_s and δt are the speed of sound and the time interval, respectively.

The sub-intermediate macroscopic variables at the interface can then be obtained by solving Eq. with finite difference method, where the discretization scheme of Eq. can be found in the previous work [64].

Through the second-order Taylor series expansion [62], the flux terms in Eqs. (3b)–(3d) can be obtained through the sub-intermediate macroscopic variables as:

$$P_\alpha=\left(\rho u_\alpha\right)^*, \tag{6a}$$

$$\begin{aligned}\Pi_{\alpha\beta}=&\left(\rho u_\alpha u_\beta+\rho c_s^2\delta_{\alpha\beta}\right)^*-\nu\left[\partial_\beta\left(\rho u_\alpha\right)+\partial_\alpha\left(\rho u_\beta\right)+\partial_\gamma\left(\rho u_\gamma\right)\delta_{\alpha\beta}\right]\\&-\left(\tau_f-0.5\right)\left[\left(\rho u_\alpha u_\beta+\rho c_s^2\delta_{\alpha\beta}\right)^*-\left(\rho u_\alpha u_\beta+\rho c_s^2\delta_{\alpha\beta}\right)\right]+O\left(\delta t^2\right),\end{aligned} \tag{6b}$$

$$\begin{aligned}Q_\alpha=&\left(\rho c_pu_\alpha T\right)^*-\chi\partial_\alpha\left(\rho c_pT\right)-\left(\tau_g-0.5\right)\left[\left(\rho c_pu_\alpha T\right)^*-\left(\rho c_pu_\alpha T\right)\right]\\&+O\left(\delta t^2\right),\end{aligned} \tag{6c}$$

where $\nu=\left(\tau_f-0.5\right)c_s^2\delta t$ and $\chi=\left(\tau_g-0.5\right)c_s^2\delta t$. τ_f and τ_g are the relaxation parameters related to the ν and χ, respectively.

Finally, the updated flow variables ρ^{n+1}, $\mathbf{u}^m$, and T^m at cell centers can be directly evaluated:

$$\rho^{n+1}=\rho^n-\frac{\Delta t}{\Delta V}\sum_k P_\alpha\Delta S_k n_{k\alpha}, \tag{7a}$$

$$\left(\rho u_\alpha\right)^m=\left(\rho u_\alpha\right)^n+\frac{\Delta t}{\Delta V}\sum_k\Pi_{\alpha\beta}\Delta S_k n_{k\beta}+F_B, \tag{7b}$$

$$\left(\rho c_pT\right)^m=\left(\rho c_pT\right)^n-\frac{\Delta t}{\Delta V}\sum_k Q_\alpha\Delta S_k n_{k\alpha}, \tag{7c}$$

where ΔV and Δt are the volume of the control cell and the macroscopic time interval, respectively. ΔS_k is the area of the kth cell interface.

2.3. IBM for Dirichlet boundary conditions

In this section, the two-dimensional IBM for Dirichlet boundary condition is introduced to correct the velocity field obtained from the intermediate flow field in the corrector step. The velocity satisfying the no-slip boundary condition can be written as:

$$\mathbf{u}^{n+1}=\mathbf{u}^m+\Delta\mathbf{u}, \tag{8}$$

where $\Delta\mathbf{u}$ is the velocity correction on the Eulerian points. Consequently, the restoring force term in the momentum equation can be written as:

$$\mathbf{f}=\rho^{n+1}\frac{\Delta\mathbf{u}}{\Delta t}. \tag{9}$$

Since the IBM for Dirichlet boundary conditions has been developed in our previous works, the details in evaluating $\Delta\mathbf{u}$ can be found in [21,23] and will not be presented here.

3. The boundary condition-enforced IBM for Robin boundary conditions

In this section, a novel boundary condition-enforced immersed boundary method for Robin boundary condition is proposed. The proposed method is capable of correcting the temperature field to accurately satisfy the Robin boundary condition on the solid wall. The corrected temperature can be obtained through the following relationship as:

$$T^{n+1}=T^m+\Delta T, \tag{10}$$

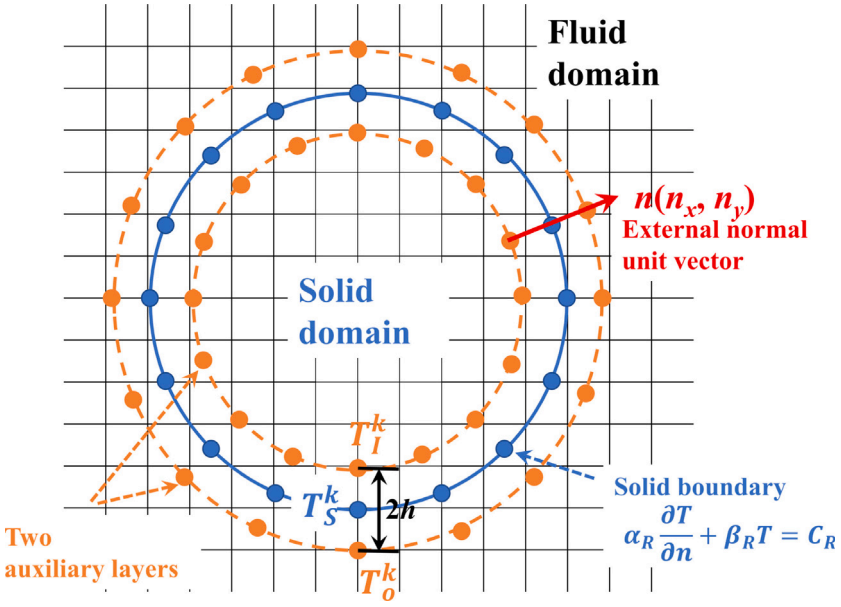

Fig. 2. Illustration of the immersed boundary method for Robin boundary conditions. The two yellow circles denote the auxiliary layers, and the blue line represents the solid boundary. The Robin boundary condition is imposed on the solid boundary, and the Lagrangian points on these three layers are distributed along the external normal direction.

where ΔT is the temperature correction at the Eulerian points. The heating source term in the energy equation can be given as:

$$q = \rho^{n+1} c_p \frac{\Delta T}{\Delta t}. \tag{11}$$

The general Robin boundary condition can be expressed as:

$$\alpha_R \left(\frac{\partial T}{\partial n} \right) + \beta_R T = C_R, \tag{12}$$

where α_R, β_R, and C_R are the parameters related to the Robin boundary condition. The scheme of the proposed IBM for Robin boundary condition is shown in Fig. 2, where two auxiliary layers shown in Fig. 2 as yellow dotted lines are introduced to encompass the solid wall such that the temperature gradient on the solid boundary can be obtained with the center difference scheme. Thereby, the general Robin boundary condition of Eq. (12) can be discretized as:

$$\frac{\alpha_R}{2h} \left(T_O^k - T_I^k \right) + \beta_R T_S^k = C_R, \tag{13}$$

where T_O^k, T_S^k, and T_I^k denote the kth temperature on the outer, middle, and inner layers, respectively, and they are given as:

$$T_\zeta^k = T_\zeta^{mk} + \delta T_\zeta^k, \quad \zeta = O, S, I, \tag{14}$$

where T_ζ^{mk} denotes the intermediate temperatures on the three layers. Substituting Eq. (14) into Eq. (13) yields the following expression:

$$\begin{aligned} &\frac{\alpha_R}{2h} \left(\delta T_O^k \left(\boldsymbol{X}_O \right) - \delta T_I^k \left(\boldsymbol{X}_I \right) \right) + \beta_R \delta T_S^k \left(\boldsymbol{X}_S \right) \\ &\quad = C_R - \frac{\alpha_R}{2h} \left(T_O^{mk} - T_I^{mk} \right) - \beta_R T_S^{mk}. \end{aligned} \tag{15}$$

The intermediate temperature on the three layers can be obtained by:

$$T_\zeta^{mk} \left(\boldsymbol{X}_\zeta \right) = \sum_j T^m \left(\boldsymbol{x}_j \right) \cdot D \left(\boldsymbol{x}_j - \boldsymbol{X}_\zeta^k \right) \cdot h^2, \quad \zeta = O, S, I. \tag{16}$$

Note that the delta function in the IBM for Robin boundary condition adopts the 3-point discrete delta function [65] as:

$$\delta(r) = \begin{cases} \left[1 + \sqrt{1 - 3(r/h)^2} \right] /3, & |r| \le 0.5h, \\ \left[5 - 3|r|/h - \sqrt{1 - 3(1 - |r|/h)^2} \right] /6, & 0.5h < |r| \le 1.5h, \\ 0, & |r| \ge 1.5h. \end{cases} \tag{17}$$

Similarly, the temperature corrections on the three layers can be evaluated through the following interpolation relationships:

$$\delta T_\zeta^k \left(\boldsymbol{X}_\zeta \right) = \sum_j \Delta T \left(\boldsymbol{x}_j \right) \cdot D \left(\boldsymbol{x}_j - \boldsymbol{X}_\zeta^k \right) \cdot h^2, \quad \zeta = O, S, I. \tag{18}$$

The scheme of the temperature correction distribution to the Eulerian points is crucial for successfully imposing the boundary condition on the immersed objects. Besides, Ji et al. [61] pointed that the biased distribution of the restoring force term is able to provide a more accurate solution for the Dirichlet boundary condition. This is because the double-sided distribution might pollute the field outside the solid domain. Hence, the biased distribution is implemented in the present IBM for Robin boundary condition, where the temperature correction on the inner layer is adopted as the heat source. It can be mathematically expressed as:

$$\Delta T \left(\boldsymbol{x}_j \right) = \begin{cases} \sum_k \left(\delta T_I^k \right) \cdot D \left(\boldsymbol{x}_j - \boldsymbol{X}_I^k \right) \cdot \Delta s_I^k, & \text{for } \boldsymbol{x}_j \text{ inside the inner layer}, \\ 0, & \text{elsewhere}, \end{cases} \tag{19}$$

where Δs_I^k represent the kth arc-length on the inner layer.

Substituting Eqs. (16), (18), and (19) into Eq. (15) yields the following relationship:

$$\begin{aligned} &C_R - \frac{\alpha_R}{2h} \left(T_O^{mk} - T_I^{mk} \right) - \beta_R T_S^{mk} \\ =&\frac{\alpha_R}{2h} \left(\sum_j \Delta T \left(\boldsymbol{x}_j \right) \cdot \left(D \left(\boldsymbol{x}_j - \boldsymbol{X}_O^k \right) - D \left(\boldsymbol{x}_j - \boldsymbol{X}_I^k \right) \right) \cdot h^2 \right) \\ &+ \beta_R \left(\sum_j \Delta T \left(\boldsymbol{x}_j \right) \cdot D \left(\boldsymbol{x}_j - \boldsymbol{X}_S^k \right) \cdot h^2 \right) \\ =&\frac{\alpha_R}{2h} \left(\sum_j \left(\sum_l \left(\delta T_I^l \cdot \Delta s^l \right) \cdot D \left(\boldsymbol{x}_j - \boldsymbol{X}_I^l \right) \right) \cdot \right. \\ &\left. \left(D \left(\boldsymbol{x}_j - \boldsymbol{X}_O^k \right) - D \left(\boldsymbol{x}_j - \boldsymbol{X}_I^k \right) \right) \cdot h^2 \right) \\ &+ \beta_R \left(\sum_j \left(\sum_l \left(\delta T_I^l \cdot \Delta s^l \right) \cdot D \left(\boldsymbol{x}_j - \boldsymbol{X}_I^l \right) \right) \cdot D \left(\boldsymbol{x}_j - \boldsymbol{X}_S^k \right) \cdot h^2 \right), \end{aligned} \tag{20}$$

which can be rewritten in the matrix form as follow:

$$\boldsymbol{C}\boldsymbol{Y} = \boldsymbol{E}, \tag{21a}$$

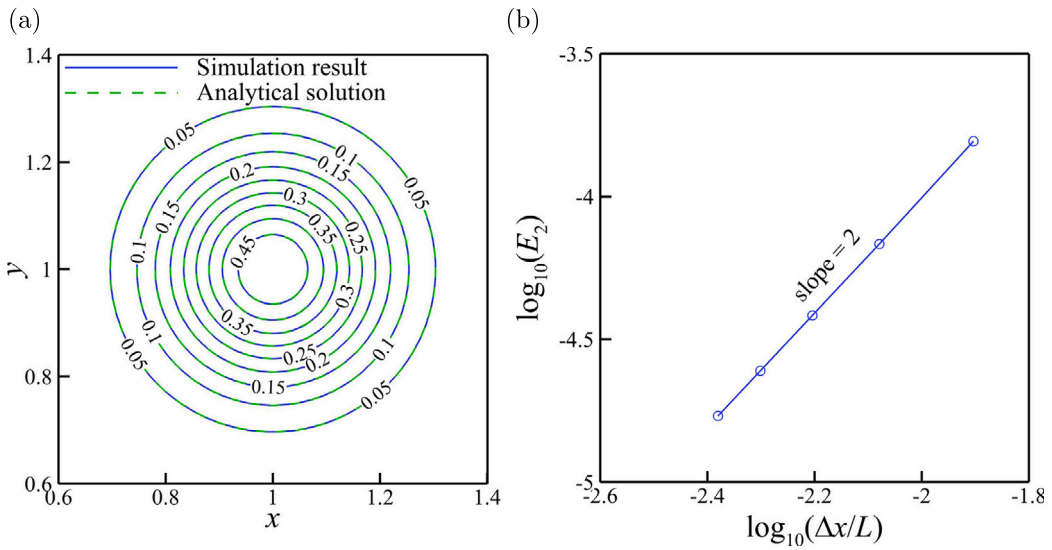

Fig. 3. (a) Comparison of the isotherms of simulated results (blue solid line) and analytical solution (green dash line) at $F_o = 0.005$. (b) Convergence of numerical error versus mesh spacing for unsteady heat diffusion of a Gaussian hill, indicating that the overall accuracy of the proposed method is of second-order.

$$C_{kl} = \sum_j \left[\frac{\alpha_R}{2h} \cdot D_I^l \cdot \left(D_O^k - D_I^k \right) + \beta_R \cdot D_I^l \cdot D_S^k \right] \cdot h^2, \tag{21b}$$

$$E_k = C_R - \frac{\alpha_R}{2h} \left(T_O^{mk} - T_I^{mk} \right) - \beta_R T_S^{mk}, \tag{21c}$$

$$\boldsymbol{Y} = \left[\delta T_I^1 \cdot \Delta s^1, \ldots, \delta T_I^l \cdot \Delta s^l, \ldots, \delta T_I^N \cdot \Delta s^N \right]^t. \tag{21d}$$

The term $\delta T_I^l \cdot \Delta s^l$ can be regarded as an unknown term, indicating that the arc-length is not taken into calculation and the accuracy of the present IBM is not associated with the arc-length. The unknown term can be directly obtained by solving the linear system shown in Eq. (21a). Therefore, the Robin boundary condition can be accurately satisfied on the immersed objects after correcting the temperature field using the proposed IBM.

4. Numerical results and validations

In this section, we assessed the overall accuracy of the boundary condition-enforced IBM for Robin boundary condition coupled with RTLBFS through the transient heat diffusion of a Gaussian hill. In addition, the capability and robustness of the proposed IBM for Robin boundary condition are evaluated with stationary and moving TFSI problems. Furthermore, the suitability of the proposed IBM for imposing Robin boundary condition on moving objects with complex geometries is examined. Lastly, the proposed IBM is applied to simulate three-dimensional moving objects with Robin boundary condition.

4.1. Examination numerical accuracy

To analyze the convergence of IBM for Dirichlet boundary condition, two-dimensional decaying vortex flow is adopted in previous studies [7,11,21,66], in which a circular cylinder is immersed in the domain center with analytical velocity being imposed on the solid surface. Then, the convergence of L_2 norm of relative error versus grid spacing can be presented to analyze.

Similarly, the transient heat diffusion of a Gaussian hill is adopted to study the overall accuracy of the proposed method, where the analytical parameter C_R of Robin boundary condition is imposed on the immersed object. The parameters of Robin boundary condition are set as: $\alpha_R = -1$ and $\beta_R = 1$. With the analytical temperature and its gradient on the solid boundary, C_R^k can be obtained as:

$$C_R^k = \frac{\alpha_R}{2h} \left(T_O^{k,exact} - T_I^{k,exact} \right) + \beta_R T_S^{k,exact}, \tag{22}$$

where $\epsilon exact\epsilon$ represents the analytical value. In this test, the computational domain is set as $[0, 2L]\times[0, 2L]$ with periodic boundary condition being imposed on all four sides. A circular cylinder with a radius of $0.25L$ is placed at the center of the computational domain and the analytical C_R is being imposed on the boundary. The initial velocity field is set as $\mathbf{u} = (u_0, 0)$ and the initial temperature field is governed by the following formula:

$$T(\mathbf{x}, 0) = \frac{T_{ref}}{2\pi\sigma^2} \exp\left[\frac{-\left(\mathbf{x} - \mathbf{X}_c\right)^2}{2\sigma^2} \right], \tag{23}$$

where T_{ref} and $\mathbf{X_c}$ denote the reference temperature and the Gaussian hill center, respectively. In this test, $\sigma = 0.05L, T_{ref} = 2\pi\sigma^2$, and $\mathbf{X}_c = (0.5L, 0)$ are employed. The analytical temperature field is given as:

$$T(\mathbf{x}, t) = \frac{T_c}{2\pi\left(2\chi t + \sigma^2\right)} \exp\left[\frac{-\left(\mathbf{x} - \mathbf{X}_c - \mathbf{u}t\right)^2}{2\left(2\chi t + \sigma^2\right)} \right]. \tag{24}$$

Five uniform meshes with spacing varying from $L/80$ to $L/240$ are setup with identical $\Delta t = 1$ and $Pe = u_0 L/\chi = 100$ to assess the numerical accuracy of the proposed method. The relative error is evaluated at $F_o = 0.005$ with the following formula as:

$$E_2 = \sqrt{\frac{\sum_{i=1}^{N} \left(T^{numerical} - T^{exact} \right)^2}{N}}, \tag{25}$$

where $\epsilon numerical\epsilon$ denotes the numerical solution and N is the total grid number on the Eulerian mesh. Fig. 3(a) shows that the isotherms obtained from present simulation are in excellent agreement with the analytical solution, where the two solutions are on top of each other. The overall spatial accuracy of the proposed method is of second order, as shown in Fig. 3(b), indicating that the effects induced by the proposed IBM for Robin boundary condition on the global accuracy is negligible.

4.2. Heat transfer around a stationary cylinder with Robin boundary condition

In this section, flows and heat transfer over a stationary circular cylinder is simulated to test the capability of the proposed solver for handling Robin boundary conditions. This type of problem is governed by Reynolds and Prandtl numbers, and they are defined as:

$$Re = \frac{U_0 D}{\nu}, \tag{26a}$$

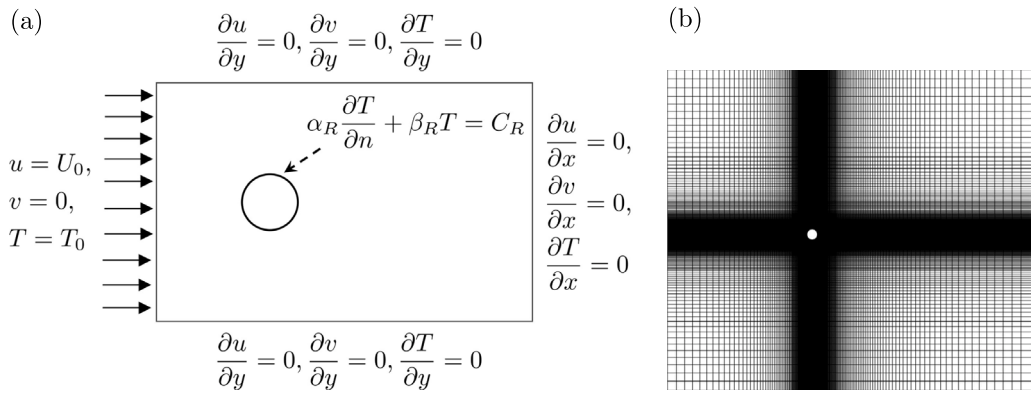

Fig. 4. (a) Overview of the computational setup of a circular cylinder with Robin boundary conditions in a free stream, where the free stream velocity U_0 and constant temperature T_0 are applied on the inlet boundary. (b) Configurations of the non-uniform mesh, where the domain around the heated cylinder is discretized by the finest mesh, where the white circle denotes the heated cylinder.

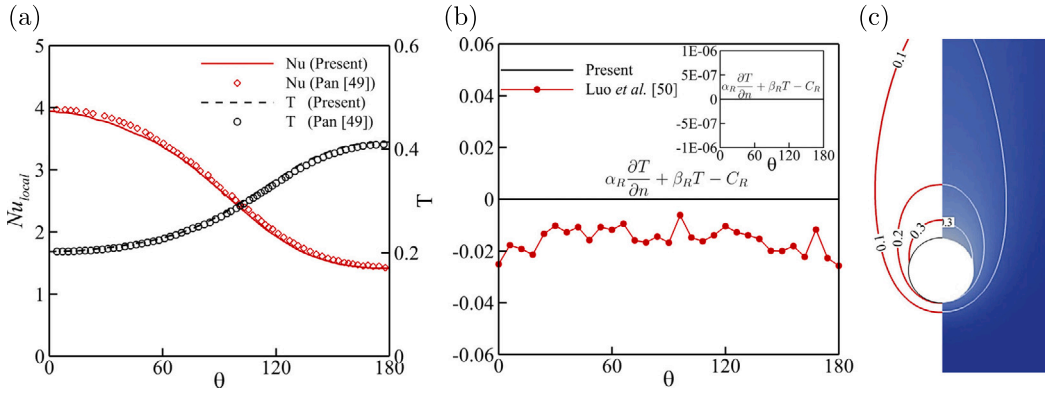

Fig. 5. (a) Local Nusselt number and temperature on the cylinder surface at $Re = 20$. (b) The error of Robin boundary condition on the cylinder surface. (c) Comparisons between isotherms of the mixed heat transfer from a heated circular cylinder with Robin boundary condition provided by Ou et al. [60] (right part of the figure) and the present results (left part of the figure) at $Re = 20$. These results obtained by the proposed boundary condition-enforced IBM for Robin boundary conditions agree well with previous studies, demonstrating the accuracy and feasibility of the proposed IBM.

$$Pr = \frac{\nu}{\chi}, \tag{26b}$$

respectively. U_0 denotes the flow velocity of the free stream and D represents the diameter of the heated circular cylinder. The computational setup is shown in Fig. 4(a), where the free stream velocity U_0 and constant temperature T_0 are applied on the inlet boundary. The computational domain (see Fig. 4(b)) is set as $[-14D, 20D]\times[-15D, 15D]$ with a mesh size of 700 × 900, where the flow region around the heated cylinder $[-1D, 4D] \times [-4D, 4D]$ is discretized uniformly with a mesh spacing of $h = 0.01D$ to capture the dynamic interaction around the cylinder and its wake region. In this case, the Prandtl number is fixed at $Pr = 0.71$ while the Reynolds number is varied from 20 to 200. No slip boundary condition and thermal Robin boundary condition are enforced at the solid wall. The local Nusselt number Nu_{local} and averaged Nusselt number Nu for measuring the heat transfer rate on the cylinder surface are defined as:

$$Nu_{local} = -\left(\frac{\partial T}{\partial n}\right)\frac{D}{T - T_0}, \tag{27a}$$

$$Nu = \frac{1}{\pi D}\sum Nu_{local} \cdot \Delta s, \tag{27b}$$

respectively. The parameters related to Robin boundary condition are specified as: $\alpha_R = -1$, $\beta_R = 1$, and $C_R = 1$.

Fig. 5(a) shows the local Nusselt number and temperature on the cylinder surface at $Re = 20$, where the present results are in good agreement with previous work of Pan [49], indicating the feasibility of the proposed IBM to implement Robin boundary condition.

The relative error of the Robin boundary condition on the solid surface is computed and shown in Fig. 5(b) to ensure that the Robin boundary condition is satisfied at the solid boundary. Interestingly, the proposed method has a much higher accuracy in satisfying the Robin boundary condition when compared to previous work of Luo et al. [50]. In addition, the isotherms around the heat cylinder obtained from present study agree well with Ou et al. [60], as shown in Fig. 5(c).

Furthermore, quantitative comparisons of the averaged Nusselt numbers tabulated in Table 1 further demonstrate the feasibility of the proposed method to accurately impose the Robin boundary condition, where the averaged Nusselt numbers obtained from present study agree well with previous studies [34,49,50].

4.3. Heat transfer around an in-line oscillating cylinder with Robin boundary condition

An in-line oscillating heated cylinder in a free stream is simulated in this section to test the capability of the proposed IBM to accurately capture the dynamic response in moving boundary problems. This

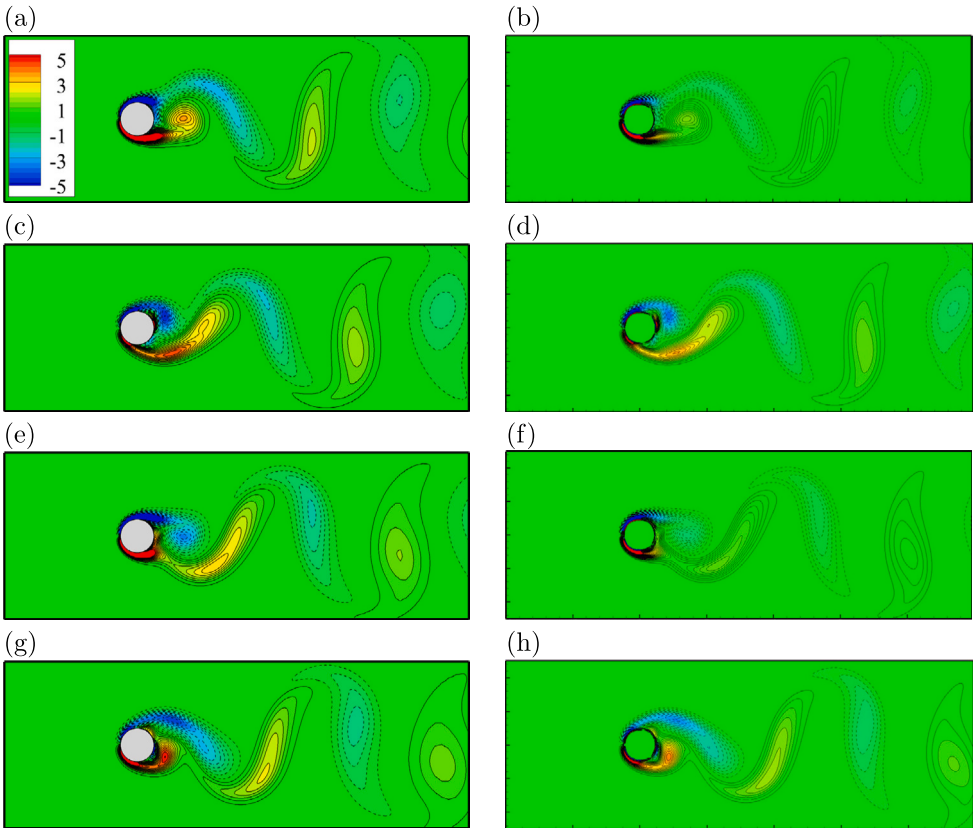

Fig. 6. Comparisons between instantaneous vorticity contours around the in-line oscillating heated cylinder provided by Luo et al. [50] (right column) and the present results (left column) at $Re = 100$. (a)–(b) $t = 0.25T_c$, (c)–(d) $t = 0.5T_c$, (e)–(f) $t = 0.75T_c$, (g)–(h) $t = T_c$. All instantaneous vorticity contours show that the present results obtained by the proposed IBM agree well with those of Luo et al. [50].

Table 1
Comparisons of the averaged Nusselt number on the cylinder surface with Robin boundary condition at different Reynolds numbers.

Re	Nu			
	Present	Hu et al. [34]	Pan [49]	Luo et al. [50]
20	**2.6733**	2.7113	2.7202	2.7221
40	**3.6317**	3.6735	3.7078	3.6532
100	**5.8396**	5.7807	5.9255	5.9161
200	**8.4668**	8.1983	8.9353	N/A

numerical test case is an extension of the numerical test case presented in Section 4.2, where an oscillating motion is applied to the cylinder. Hence, the computational domain, mesh spacing, and boundary conditions are identical to those adopted in Section 4.2 with $Re = 100$ and $Pr = 0.7$ being adopted in this numerical test case. The oscillating motion is governed by:

$$X_c(t) = A\sin\left(2\pi f_c t\right), \tag{28}$$

where A denotes the oscillating amplitude and is set as $A/D = 0.14$. f_c represents the oscillating frequency and is set to be $f_c = 2f_0$, where f_0 denotes the vortex shedding frequency of a stationary cylinder at $Re = 100$. The oscillating period is defined as $T_c = 1/f_c$ and the parameters related to the Robin boundary condition are the same as those applied in Luo et al. [50].

Figs. 6 and 7 show the comparisons between the vorticity contours and the isotherms of an in-line oscillating heated cylinder obtained by Luo et al. [50] and the present results at four time instants. It can be seen that the results obtained by the proposed IBM for Robin boundary condition agree quite well with that of Luo et al. [50], qualitatively demonstrating the capability of the proposed IBM for imposing the Robin boundary condition on the solid boundary.

The comparisons of the time histories of the drag coefficient, lift coefficient, and averaged Nusselt number are shown in Fig. 8 to further assess the accuracy and capability of the proposed method. It is evident from Fig. 8 that the present results agree well with the reference data from Luo et al. [50], demonstrating that the nonlinear dynamic characteristics are captured accurately by the proposed IBM. Note that the small discrepancies observed in the averaged Nusselt number between Luo et al. [50] and the present study might be induced by the errors introduced by different interpolation schemes. In addition, the instantaneous distributions of temperature, temperature gradient, local Nusselt number, and the errors of Robin boundary condition are presented in Fig. 9 at four identical time instants used in Figs. 6 and 7. As shown in Figs. 9(a)–(c), the distribution of the temperature and its gradient are opposite in trends, indicating that the local Nusselt number reaches its maximum value at windward point, while the minimum value is associated to the vortex shedding position. The instantaneous errors of the Robin boundary condition (see Fig. 9(d)) on the immersed boundary are negligible, demonstrating that the proposed IBM can accurately impose Robin boundary condition on the surface of moving objects and highlighting its flexibility of imposing Robin boundary condition.

4.4. Heat transfer around a heaving airfoil with Robin boundary condition

Forced convection flows past a heaving heated airfoil with imposed Robin boundary conditions are considered in this section to examine the capability of the proposed IBM for handling TFSI problems with complex geometries and moving boundaries. The numerical setup is slightly different from previous section, where a free stream velocity U_0 and a constant temperature T_0 are imposed on the inlet boundary, while zero gradient Neumann boundary condition is applied to the remaining

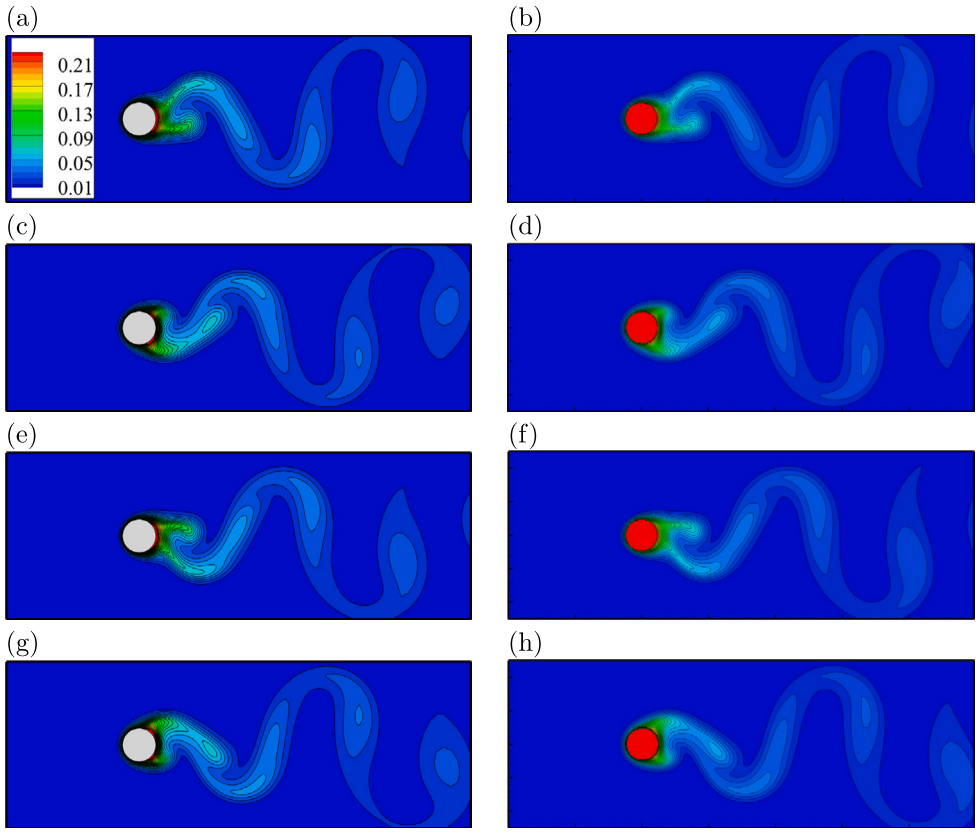

Fig. 7. Comparisons between instantaneous isotherms around the in-line oscillating heated cylinder provided by Luo et al. [50] (right column) and the present results (left column) at $Re = 100$. (a)–(b) $t = 0.25T_c$, (c)–(d) $t = 0.5T_c$, (e)–(f) $t = 0.75T_c$, (g)–(h) $t = T_c$. All instantaneous temperature isotherms show that the present results obtained by the proposed IBM agree well with those of Luo et al. [50].

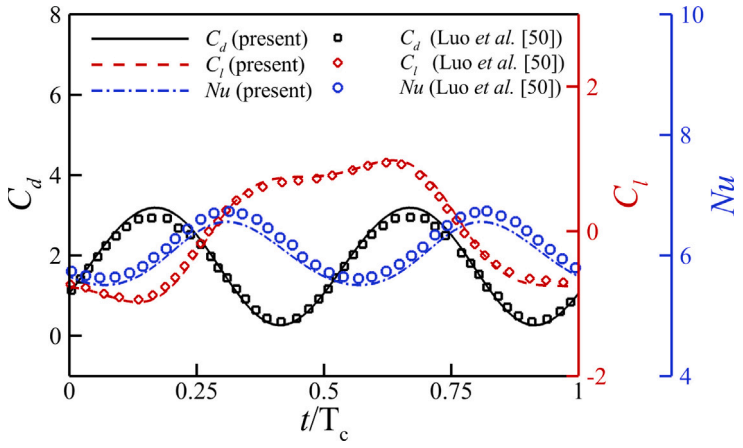

Fig. 8. Comparisons of the time variations of the drag coefficient, lift coefficient, and averaged Nusselt number for in-line oscillating cylinder with Robin boundary condition at $Re = 100$ and $f_c/f_0 = 2$. It quantitatively demonstrates that the present results obtained by the proposed IBM agree with those in previous work [50], indicating the feasibility of the proposed numerical approach.

boundaries. The selected airfoil for this test case takes the shape of an ellipse with a thickness to chord length ratio ($\epsilon = e/c$) of 1/8. The heaving motion of the airfoil is governed by:

$$h(t) = h_0 \sin(2\pi f t), \tag{29}$$

where h_0 denotes the oscillating amplitude and f is the heaving frequency. The heaving period is $T_c = 1/f$.

This numerical test is governed by the following dimensionless group: Reynolds number ($Re = \frac{U_0 c}{\nu} = 500$), Prandtl number ($Pr = \frac{\nu}{\chi} = 0.7$), and two variants of Strouhal numbers ($St_a = \frac{h_0 f}{U_0} = 0.16$ and $St_c = \frac{cf}{U_0} = 0.5$). The thermal Robin boundary condition is imposed on the airfoil surface with $\alpha_R = -1$, $\beta_R = 1$, and $C_R = 1$. Note that the effects of natural convection and internal heat are neglected in this study.

The local Nusselt number Nu_{local} and average Nusselt number Nu for measuring the heat transfer rate on the airfoil surface are defined as:

$$Nu_{local} = -\left(\frac{\partial T}{\partial n}\right)\frac{c}{T - T_0}, \tag{30a}$$

$$Nu = \frac{1}{\sum \Delta s}\sum Nu_{local} \cdot \Delta s, \tag{30b}$$

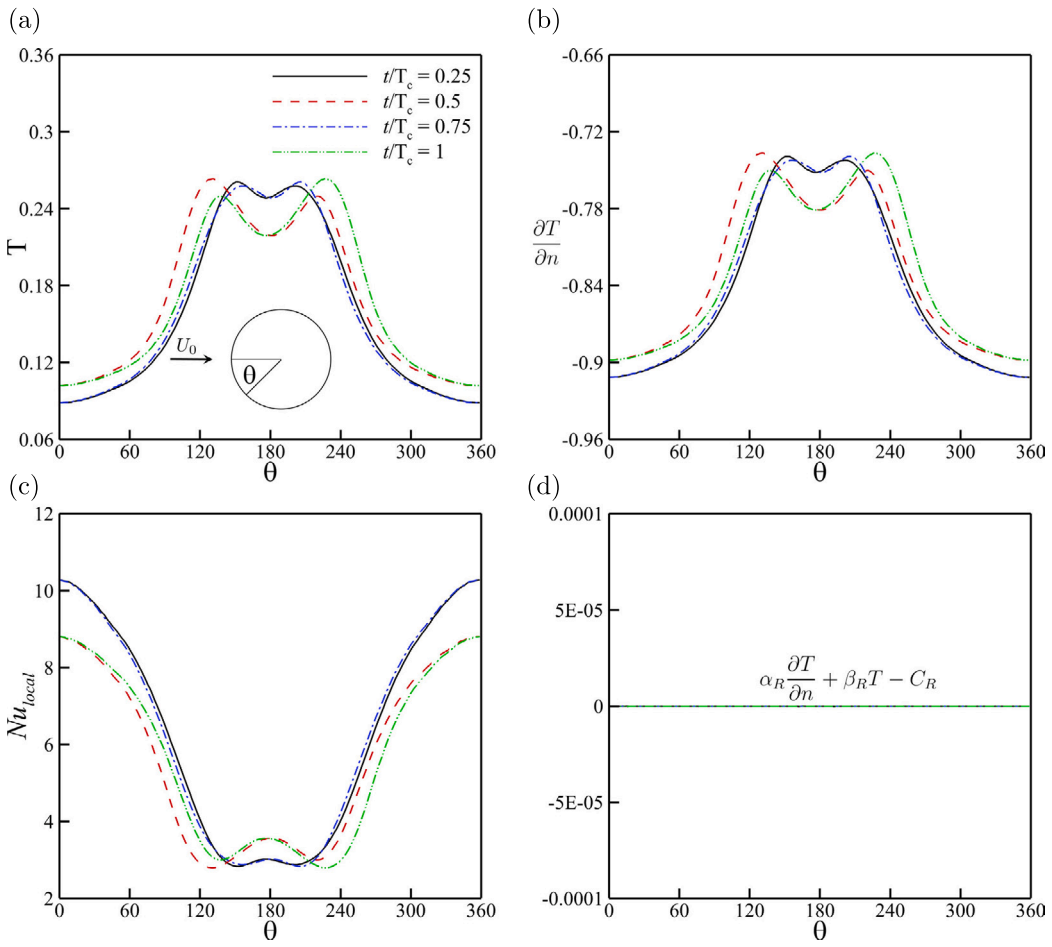

Fig. 9. The distributions of (a) temperature, (b) temperature gradient, (c) local Nusselt number, and (d) the errors of Robin boundary condition on the immersed boundary at four time instants. The errors of Robin boundary condition quantitatively demonstrates that the proposed IBM can accurately imposed the Robin boundary condition on the solid boundary.

respectively. The computational domain is set as $[-5c, 13c] \times [-6c, 6c]$ with a mesh size of 1000 × 900, where the flow region around the airfoil $[-c, 3c] \times [-2c, 2c]$ is discretized uniformly with a finer mesh spacing of $h = 0.005c$ to capture accurately the dynamic interaction around the airfoil and its wake region.

Fig. 10 shows the vorticity contours and isotherms around the heaving heated airfoil at different time instants. It can be seen that the instantaneous vorticity contours are consistent with those reported in Martín-Alcántara et al. [67], thereby, qualitatively demonstrating that the present solver can accurately capture the vortex dynamics around the heaving airfoil. It is also evident from Fig. 10 that the isotherms around the airfoil is closely related to the vortex configurations, indicating that the heat transfer rate is highly correlated with the vorticity field. Fig. 11(a) shows that the drag coefficient and averaged Nusselt number obtained from present study are in good agreement with previous works [67,68], further demonstrating the accuracy and robustness of the proposed method for solving complex problems related to moving objects. As shown in Fig. 11(b), when the airfoil achieves statistically steady oscillating state, the averaged Nusselt number fluctuates periodically.

In addition, the instantaneous distributions of temperature, temperature gradient, local Nusselt number, and the errors of Robin boundary condition are presented in Fig. 12 at the same time instants selected for Fig. 10. As expected, the location of high temperature correlates with low temperature gradient due to the constraint imposed by the Robin boundary condition. Interestingly, the local Nusselt number is relatively high around the leading edge and trailing edge. In addition, the strength of the convection is found to be much larger at the lower side when compared to the upper side, as the airfoil is heaving downwards. Opposite trend is observed when the airfoil is heaving upwards. Note that the errors of the Robin boundary condition are negligible at all time instants, as shown in Fig. 12(d), demonstrating the robustness and accuracy of the present IBM of imposing Robin boundary condition on moving objects with complex geometries.

4.5. Heat transfer around a three dimensional rotating sphere with Robin boundary condition

In this section, the flow past a heated rotating sphere with Robin boundary conditions is adopted to examine the capability of the proposed IBM for simulating 3D Robin-type TFSI problem with moving boundaries. Fig. 13 shows the schematic diagram of this problem, where the rotating axis is located along the streamwise direction (z axis). On the inlet boundary, free stream velocity U_0 and constant temperature T_0 are applied. The numerical case is governed by three dimensionless parameters: Reynolds number $Re = U_0 D/\nu$, dimensionless rotation speed $\Omega = \omega D/2U_0$, and Prandtl number $Pr = \nu/\chi$, where D and ω are the sphere diameter and rotational speed, respectively. The size of the computational domain is $24D \times 24D \times 30D$, where the region around the sphere is discretized with uniform mesh of $\Delta x = D/50$. The spherical surface is evenly discretized by 1333 Lagrangian points. In this test, the parameters: $Re = 300$, $Pr = 0.7$, $\alpha_R = -1$, $\beta_R = 1$, $C_R = 1$, and $\Omega = 0.1, 0.3$ are adopted. The time histories of the dimensionless forces exerted on the sphere and the averaged Nusselt number are presented in Fig. 14. The dimensionless force variations are in good agreement with those in previous studies [21,69], indicating that the

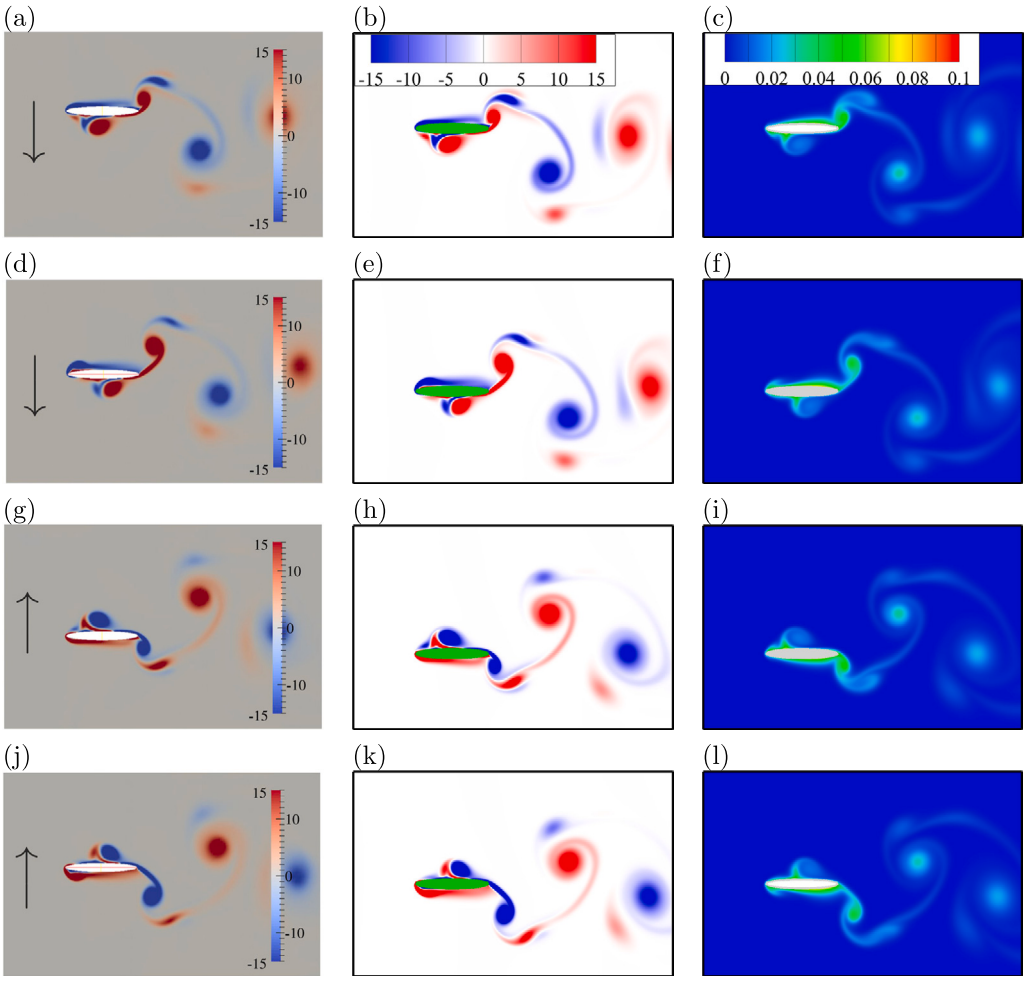

Fig. 10. Comparisons between instantaneous vorticity field around the heaving airfoil provided by Martín-Alcántara et al. [67] (left column) and the present results (middle column) at $Re = 500$, $St_a = 0.16$, and $St_c = 0.5$. The instantaneous isotherms around the heaving heated airfoil are presented at right column. (a)–(c) $t/T_c = 1/8$, (d)–(f) $t/T_c = 1/4$, (g)–(i) $t/T_c = 5/8$, and (j)–(l) $t/T_c = 3/4$. The instantaneous vorticity contours obtained by the present method agree well with those of Martín-Alcántara et al. [67], which qualitatively verify that the proposed method can accurately capture the flow structures around complex moving boundaries.

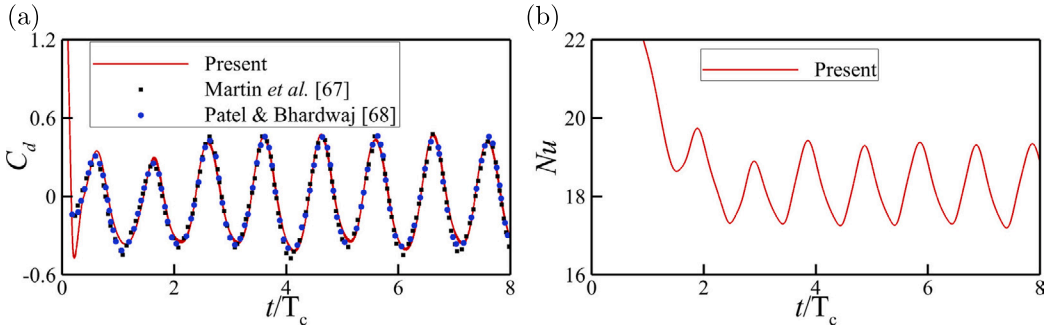

Fig. 11. (a) Comparisons between the drag coefficient provided by Martín-Alcántara et al. [67], Patel and Bhardwaj [68] and the present results. (b) The time evolution of the averaged Nusselt number, which changes periodically when the airfoil achieves stable oscillation. The comparisons quantitatively demonstrate that the numerical results obtained by the present method agree with those in previous works [67,68], indicating that the present method can accurately capture the non-linear aerodynamic forces.

present numerical approach can accurately capture the dynamic responses of 3D TFSI problems with moving boundary. Detailed results for dimensionless forces can be found in our previous work [21].

The instantaneous temperature, temperature gradient, and the errors of the Robin boundary condition are depicted in Fig. 15 to further evaluate the accuracy of the proposed IBM for Robin boundary condition. It is found that the instantaneous temperature is low while the temperature gradient is relatively high at the windward side, thereby, increasing the local Nusselt number and also the strength of convection when compared to the leeward side. It is evident from Fig. 15(c) that the errors of the Robin boundary condition are negligible, further strengthening the suitability of the proposed IBM to accurately impose the Robin boundary condition on immersed object.

5. Conclusions

In this work, a novel boundary condition-enforced IBM for effectively imposing Robin boundary conditions on immersed objects has

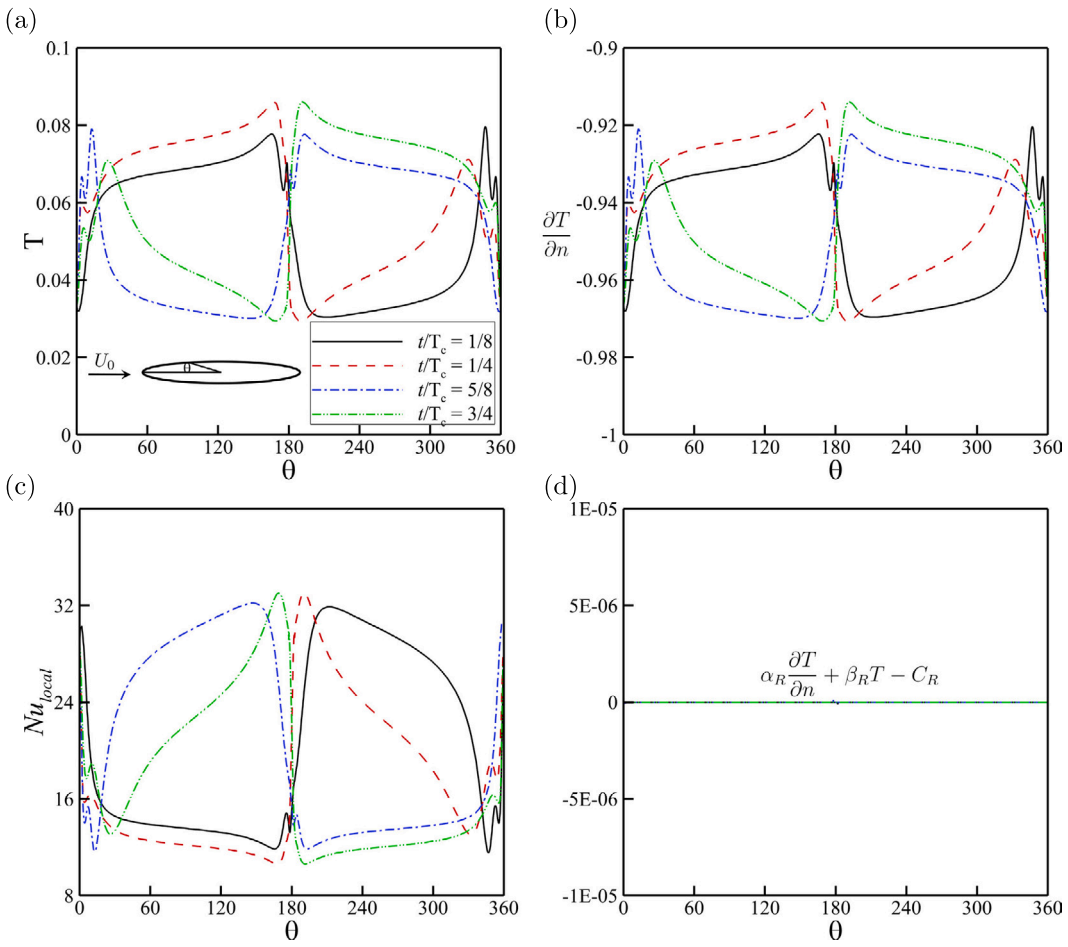

Fig. 12. The distributions of (a) temperature, (b) temperature gradient, (c) local Nusselt number, and (d) the errors of Robin boundary condition at the time instants corresponding to Fig. 10. The errors of Robin boundary condition quantitatively demonstrates that the proposed IBM can accurately imposed the Robin boundary condition on the airfoil boundary.

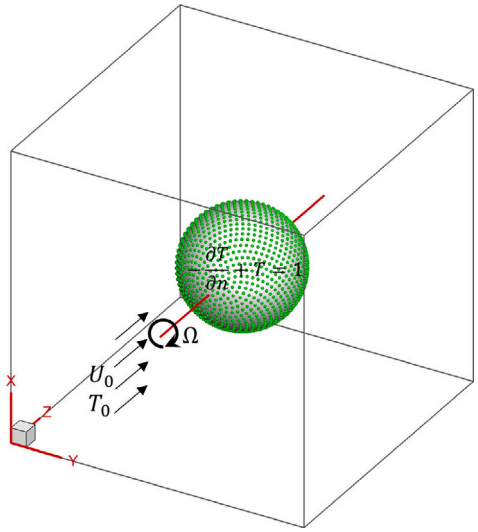

Fig. 13. Schematic diagram of flow past a rotating sphere, where the rotating axis is along the streamwise direction and the green points on the spherical surface denote the Lagrangian points. The Robin boundary condition is enforced on the spherical surface, where $\alpha_R = -1$, $\beta_R = 1$ and $C_R = 1$ are adopted.

been proposed, which is integrated with RTLBFS to simulate TFSI problems with Robin boundary conditions. Previous attempts on imposing Robin boundary conditions with IBMs rely on either the direct forcing scheme or the ghost cell scheme, where a thermal boundary forcing term is introduced to correct the temperature field, triggering that the variables on the solid boundary may have some discrepancies with the prescribed Robin boundary condition. In the present IBM, we introduced two auxiliary layers of Lagrangian points and the temperature corrections on these Lagrangian points can be implicitly resolved by accurately enforcing the Robin boundary condition on the solid boundary. Subsequently, the temperature corrections are biasedly distributed on the Eulerian points located in the inner auxiliary layer to reduce the diffusion generated by the smooth delta function on the temperature field outside the solid object.

The proposed method is demonstrated to have an overall numerical accuracy of second-order. The proposed IBM is validated with several benchmark cases ranging from stationary immersed objects to moving boundaries. Good agreements with previous works demonstrate the feasibility and the accuracy of the proposed IBM. In addition, the present IBM has been extended to investigate TFSI problems involving complex moving boundary in three dimensional space, where the Robin boundary condition is found to be accurately enforced by the proposed method. Most importantly, all benchmark cases show that the errors of Robin boundary conditions enforced by the proposed IBM are negligible. Therefore, the proposed IBM can be used to effectively and accurately resolve various TFSI problems involving Robin boundary conditions. Consistent with the boundary condition-enforced IBM for Dirichlet boundary conditions [7,70], the proposed IBM for Robin boundary conditions can be easily coupled with LBM and N-S solvers to solve Robin-type TFSI problems.

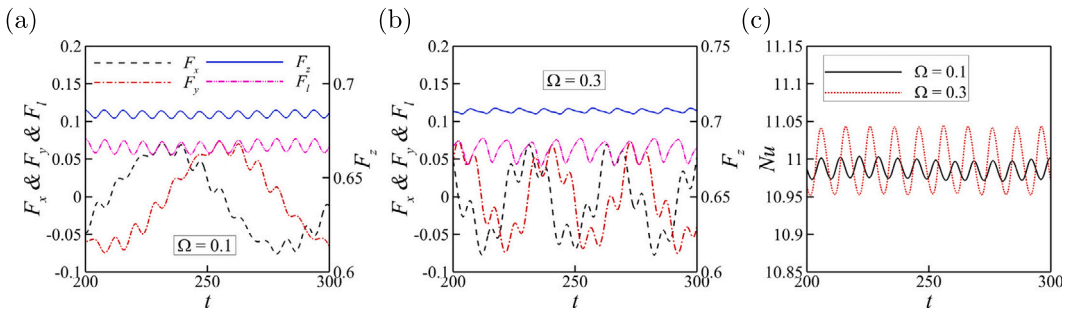

Fig. 14. The time histories of the dimensionless forces on the sphere at (a) $\Omega = 0.1$ and (b) $\Omega = 0.3$. (c) The time histories of the averaged Nusselts number on the sphere with Robin boundary condition. F_x, F_y, and F_z denote the force components along the x, y, and z axis, respectively. The lift force is defined as $F_l = \sqrt{F_x^2 + F_y^2}$ and the averaged Nusselt number is defined as $Nu = \frac{1}{\sum \Delta s} \sum \left(-\left(\frac{\partial T}{\partial n}\right) \frac{D}{T - T_0}\right) \cdot \Delta s$.

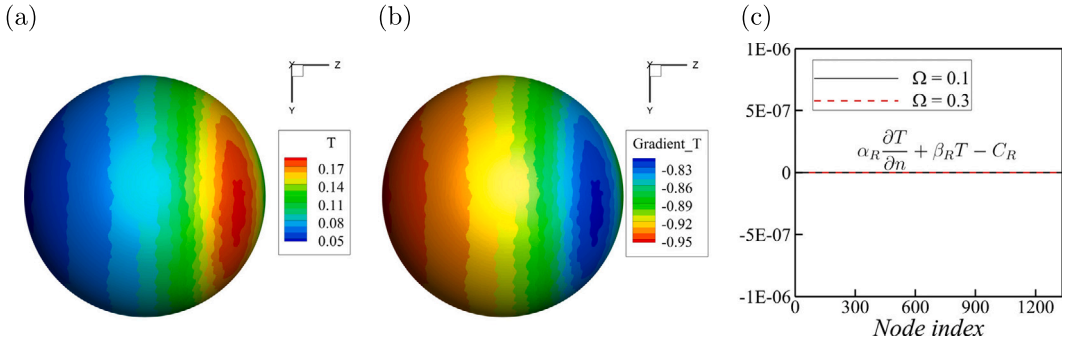

Fig. 15. The instantaneous distributions of (a) temperature and (b) temperature gradient on the spherical surface at $Re = 300$ and $\Omega = 0.1$. (c) The errors of the Robin boundary condition at the Lagrangian points when $\Omega = 0.1, 0.3$. The errors of Robin boundary condition quantitatively demonstrates that the proposed IBM can accurately imposed the Robin boundary condition on 3D complex moving boundaries.

CRediT authorship contribution statement

Buchen Wu: Conceptualization, Methodology, Software, Validation, Writing – original draft. **Chang Shu:** Formal analysis, Supervision, Writing – original draft. **Minping Wan:** Formal analysis, Supervision, Writing – original draft.

Declaration of competing interest

The authors declare that they have no known competing financial interests or personal relationships that could have appeared to influence the work reported in this paper.

Data availability

Data will be made available on request.

Acknowledgments

This work has been supported by the Key-Area Research and Development Program of Guangdong Province, China (Grant No. 2021B0101190003), the Department of Science and Technology of Guangdong Province, China (Grant No. 2020B1212030001), and the Shenzhen Science & Technology Program, China (Grant No. KQTD20180411143441009). Numerical simulations have been supported by the Center for Computational Science and Engineering of Southern University of Science and Technology, China.

References

[1] Mittal R, Iaccarino G. Immersed boundary methods. Annu Rev Fluid Mech 2005;37:239–61.
[2] Sotiropoulos F, Yang X. Immersed boundary methods for simulating fluid–structure interaction. Prog Aerosp Sci 2014;65:1–21.
[3] Huang W-X, Tian F-B. Recent trends and progress in the immersed boundary method. Proc Inst Mech Eng C 2019;233(23–24):7617–36.
[4] Mittal R, Bhardwaj R. Immersed boundary methods for thermofluids problems. Annu Rev Heat Transfer 2021;24.
[5] Verzicco R. Immersed boundary methods: Historical perspective and future outlook. Annu Rev Fluid Mech 2023;55:129–55.
[6] Peskin CS. Numerical analysis of blood flow in the heart. J Comput Phys 1977;25(3):220–52.
[7] Wu J, Shu C. Implicit velocity correction-based immersed boundary-lattice Boltzmann method and its applications. J Comput Phys 2009;228(6):1963–79.
[8] Tian F-B, Luo H, Zhu L, Liao JC, Lu X-Y. An efficient immersed boundary-lattice Boltzmann method for the hydrodynamic interaction of elastic filaments. J Comput Phys 2011;230(19):7266–83.
[9] Tian F-B, Dai H, Luo H, Doyle JF, Rousseau B. Fluid–structure interaction involving large deformations: 3D simulations and applications to biological systems. J Comput Phys 2014;258:451–69.
[10] Wang Y, Shu C, Teo C, Wu J. An immersed boundary-lattice Boltzmann flux solver and its applications to fluid–structure interaction problems. J Fluids Struct 2015;54:440–65.
[11] Zhao X, Chen Z, Yang L, Liu N, Shu C. Efficient boundary condition-enforced immersed boundary method for incompressible flows with moving boundaries. J Comput Phys 2021;110425.
[12] Goldstein D, Handler R, Sirovich L. Modeling a no-slip flow boundary with an external force field. J Comput Phys 1993;105(2):354–66.
[13] Zhu L, He G, Wang S, Miller L, Zhang X, You Q, Fang S. An immersed boundary method based on the lattice Boltzmann approach in three dimensions, with application. Comput Math Appl 2011;61(12):3506–18.
[14] Feng Z-G, Michaelides EE. The immersed boundary-lattice Boltzmann method for solving fluid–particles interaction problems. J Comput Phys 2004;195(2):602–28.

[15] De Rosis A, Ubertini S, Ubertini F. A partitioned approach for two-dimensional fluid–structure interaction problems by a coupled lattice Boltzmann-finite element method with immersed boundary. J Fluids Struct 2014;45:202–15.
[16] De Rosis A, Ubertini S, Ubertini F. A comparison between the interpolated bounce-back scheme and the immersed boundary method to treat solid boundary conditions for laminar flows in the lattice Boltzmann framework. J Sci Comput 2014;61(3):477–89.
[17] Suzuki K, Inamuro T. Effect of internal mass in the simulation of a moving body by the immersed boundary method. Comput & Fluids 2011;49(1):173–87.
[18] Niu X, Shu C, Chew Y, Peng Y. A momentum exchange-based immersed boundary-lattice Boltzmann method for simulating incompressible viscous flows. Phys Lett A 2006;354(3):173–82.
[19] Chen Y, Cai Q, Xia Z, Wang M, Chen S. Momentum-exchange method in lattice Boltzmann simulations of particle-fluid interactions. Phys Rev E 2013;88(1):013303.
[20] Chen Y, Djidjeli K, Xie Z-T. Large eddy simulation of flow past stationary and oscillating square cylinders. J Fluids Struct 2020;97:103107.
[21] Wu B, Lu J, Lee H, Shu C, Wan M. An efficient explicit immersed boundary-reconstructed lattice Boltzmann flux solver for isothermal fluid-structure interaction problems with large deformations and complex geometries. Appl Math Model 2023;114:627–45.
[22] Li Z, Oger G, Le Touzé D. A partitioned framework for coupling LBM and FEM through an implicit IBM allowing non-conforming time-steps: Application to fluid-structure interaction in biomechanics. J Comput Phys 2022;449:110786.
[23] Wu B, Lu J, Lee H, Shu C, Wan M. An explicit immersed boundary-reconstructed thermal lattice Boltzmann flux solver for thermal–fluid-structure interaction problems. Int J Mech Sci 2022;235:107704.
[24] Xu T, Choi J-I. Efficient monolithic immersed boundary projection method for incompressible flows with heat transfer. J Comput Phys 2023;477:111929.
[25] Zhang D, Li Y, Zhang J, Yuan H, Zhang Z. Pore-scale numerical study: brine water crystallization with ice crystal particle motion using the LBM-PFM-IBM. Appl Therm Eng 2023;121258.
[26] Zhang N, Zheng Z, Eckels S. Study of heat-transfer on the surface of a circular cylinder in flow using an immersed-boundary method. Int J Heat Fluid Flow 2008;29(6):1558–66.
[27] Shu C, Ren W, Yang W. Novel immersed boundary methods for thermal flow problems. Internat J Numer Methods Heat Fluid Flow 2013;23(1):124–42.
[28] Shao J, Shu C, Chew Y-T. Development of an immersed boundary-phase field-lattice Boltzmann method for Neumann boundary condition to study contact line dynamics. J Comput Phys 2013;234:8–32.
[29] Ren W, Shu C, Yang W. An efficient immersed boundary method for thermal flow problems with heat flux boundary conditions. Int J Heat Mass Transfer 2013;64:694–705.
[30] Xia J, Luo K, Fan J. A ghost-cell based high-order immersed boundary method for inter-phase heat transfer simulation. Int J Heat Mass Transfer 2014;75:302–12.
[31] Nagendra K, Tafti DK, Viswanath K. A new approach for conjugate heat transfer problems using immersed boundary method for curvilinear grid based solvers. J Comput Phys 2014;267:225–46.
[32] Hu Y, Li D, Shu S, Niu X. Study of multiple steady solutions for the 2D natural convection in a concentric horizontal annulus with a constant heat flux wall using immersed boundary-lattice Boltzmann method. Int J Heat Mass Transfer 2015;81:591–601.
[33] Wang Y, Shu C, Yang L. Boundary condition-enforced immersed boundary-lattice Boltzmann flux solver for thermal flows with Neumann boundary conditions. J Comput Phys 2016;306:237–52.
[34] Hu Y, Li D, Shu S, Niu X. An efficient immersed boundary-lattice Boltzmann method for the simulation of thermal flow problems. Commun Comput Phys 2016;20(5):1210–57.
[35] Guo T, Shen E, Lu Z, Wang Y, Dong L. Implicit heat flux correction-based immersed boundary-finite volume method for thermal flows with Neumann boundary conditions. J Comput Phys 2019;386:64–83.
[36] Lou J, Johnston J, Tilton N. Application of projection and immersed boundary methods to simulating heat and mass transport in membrane distillation. Comput & Fluids 2020;212:104711.
[37] Wu B, Lu J, Lee H, Shu C, Wan M. An explicit boundary condition-enforced immersed boundary-reconstructed thermal lattice Boltzmann flux solver for thermal-fluid-structure interaction problems with heat flux boundary conditions. J Comput Phys 2023;485:112106.
[38] Yan H, Zhang G, Xiao Y, Hui D, Wang S. A surface flux correction-based immersed boundary-multiphase lattice Boltzmann flux solver applied to multiphase fluids–structure interaction. Comput Methods Appl Mech Engrg 2022;400:115481.
[39] Chen H, Zhao H, Huang T, Yu P, Shu C. A unified numerical model for simulating heat transfer in flows past porous bodies. Internat J Numer Methods Engrg 2023.
[40] Zhao X, Yang L, Xu C, Shu C. An overset boundary condition-enforced immersed boundary method for incompressible flows with large moving boundary domains. Phys Fluids 2022;34(10).
[41] Wu J, Shu C, Zhao N, Tian F-B. Numerical study on the power extraction performance of a flapping foil with a flexible tail. Phys Fluids 2015;27(1):013602.
[42] Wu B, Shu C, Wan M, Wang Y, Chen S. Hydrodynamic performance of an unconstrained flapping swimmer with flexible fin: A numerical study. Phys Fluids 2022;34(1):011901.
[43] Wu B, Shu C, Lee H, Wan M. The effects of caudal fin's bending stiffness on a self-propelled carangiform swimmer. Phys Fluids 2022;34(4):041901.
[44] Wu B, Shu C, Lee HC, Wan M. Numerical study on the hydrodynamic performance of an unconstrained carangiform swimmer. Phys Fluids 2022;34(12):121902.
[45] Zhang H, Liu Y, Zhang Z, Wang L-P, Shu C. An immersed boundary-lattice Boltzmann flux solver for simulation of flows around structures with large deformation. Phys Fluids 2023;35(3).
[46] Xiao W, Zhang H, Luo K, Mao C, Fan J. Immersed boundary method for multiphase transport phenomena. Rev Chem Eng 2022;38(4):363–405.
[47] Tseng Y-H, Ferziger JH. A ghost-cell immersed boundary method for flow in complex geometry. J Comput Phys 2003;192(2):593–623.
[48] Pacheco-Vega A, Pacheco JR, Rodić T. A general scheme for the boundary conditions in convective and diffusive heat transfer with immersed boundary methods. J Heat Transfer 2007;129(11):1506–16.
[49] Pan D. A general boundary condition treatment in immersed boundary methods for incompressible Navier-Stokes equations with heat transfer. Numer Heat Transfer B 2012;61(4):279–97.
[50] Luo K, Zhuang Z, Fan J, Haugen NEL. A ghost-cell immersed boundary method for simulations of heat transfer in compressible flows under different boundary conditions. Int J Heat Mass Transfer 2016;92:708–17.
[51] Luo K, Mao C, Zhuang Z, Fan J, Haugen NEL. A ghost-cell immersed boundary method for the simulations of heat transfer in compressible flows under different boundary conditions Part-II: Complex geometries. Int J Heat Mass Transfer 2017;104:98–111.
[52] Yousefzadeh M, Battiato I. High order ghost-cell immersed boundary method for generalized boundary conditions. Int J Heat Mass Transfer 2019;137:585–98.
[53] Kinoshita D, Martinez Padilla EL, da Silveira Neto A, Pamplona Mariano F, Serfaty R. Fourier pseudospectral method for nonperiodical problems: A general immersed boundary method for three types of thermal boundary conditions. Numer Heat Transfer B 2016;70(6):537–58.
[54] Kumar M, Natarajan G. Diffuse-interface immersed-boundary framework for conjugate-heat-transfer problems. Phys Rev E 2019;99(5):053304.
[55] Favre F, Antepara O, Oliet C, Lehmkuhl O, Perez-Segarra CD. An immersed boundary method to conjugate heat transfer problems in complex geometries. Application to an automotive antenna. Appl Therm Eng 2019;148:907–28.
[56] Pan J-H, Ni M-J, Zhang N-M. A consistent and conservative immersed boundary method for MHD flows and moving boundary problems. J Comput Phys 2018;373:425–45.
[57] Mohd-Yusof J. Combined immersed-boundary/B-spline methods for simulations of flow in complex geometries. Cent Turbul Res Annu Res Briefs 1997;161(1):317–27.
[58] Fadlun E, Verzicco R, Orlandi P, Mohd-Yusof J. Combined immersed-boundary finite-difference methods for three-dimensional complex flow simulations. J Comput Phys 2000;161(1):35–60.
[59] Luo K, Mao C, Fan J, Zhuang Z, Haugen NEL. Fully resolved simulations of single char particle combustion using a ghost-cell immersed boundary method. AIChE J 2018;64(7):2851–63.
[60] Ou Z, Chi C, Guo L, Thévenin D. A directional ghost-cell immersed boundary method for low mach number reacting flows with interphase heat and mass transfer. J Comput Phys 2022;468:111447.
[61] Ji C, Munjiza A, Williams J. A novel iterative direct-forcing immersed boundary method and its finite volume applications. J Comput Phys 2012;231(4):1797–821.
[62] Lu J, Dai C, Yu P. Analysis and reconstruction of the thermal lattice Boltzmann flux solver. Internat J Numer Methods Fluids 2022.
[63] Gray DD, Giorgini A. The validity of the Boussinesq approximation for liquids and gases. Int J Heat Mass Transfer 1976;19(5):545–51.
[64] Lu J, Lei H, Shu C, Dai C. The more actual macroscopic equations recovered from lattice Boltzmann equation and their applications. J Comput Phys 2020;415:109546.
[65] Roma AM, Peskin CS, Berger MJ. An adaptive version of the immersed boundary method. J Comput Phys 1999;153(2):509–34.
[66] Yang L, Shu C, Yang W, Wang Y, Wu J. An immersed boundary-simplified sphere function-based gas kinetic scheme for simulation of 3D incompressible flows. Phys Fluids 2017;29(8):083605.
[67] Martín-Alcántara A, Fernandez-Feria R, Sanmiguel-Rojas E. Vortex flow structures and interactions for the optimum thrust efficiency of a heaving airfoil at different mean angles of attack. Phys Fluids 2015;27(7):073602.
[68] Patel A, Bhardwaj R. Propulsive performance of a two-dimensional elliptic foil undergoing interlinked pitching and heaving. Phys Fluids 2022.
[69] Wang Y, Shu C, Teo C, Yang L. An efficient immersed boundary-lattice Boltzmann flux solver for simulation of 3D incompressible flows with complex geometry. Comput & Fluids 2016;124:54–66.
[70] Ren W, Shu C, Wu J, Yang W. Boundary condition-enforced immersed boundary method for thermal flow problems with Dirichlet temperature condition and its applications. Comput & Fluids 2012;57:40–51.